ACS APPLIED MATERIALS & INTERFACES

Research Article

www.acsami.org

Hierarchical Ternary Carbide Nanoparticle/Carbon Nanotube-Inserted N-Doped Carbon Concave-Polyhedrons for Efficient Lithium and Sodium Storage

Tao Chen,[†] Baorui Cheng,[†] Renpeng Chen,[†] Yi Hu,[†] Hongling Lv,[†] Guoyin Zhu,[†] Yanrong Wang,[†] Lianbo Ma,[†] Jia Liang,[†] Zuoxiu Tie,[‡] Zhong Jin,*[,†] and Jie Liu*[,†,§]

[†]Key Laboratory of Mesoscopic Chemistry of MOE and Collaborative Innovation Center of Chemistry for Life Sciences, School of Chemistry and Chemical Engineering, Nanjing University, Nanjing, Jiangsu 210023, China

[‡]Department of Engineering and Applied Sciences, Nanjing University, Nanjing, Jiangsu 210023, China

[§]Department of Chemistry, Duke University, Durham, North Carolina 27708, United States

Supporting Information

ABSTRACT: Here, we report a hierarchical Co_3ZnC/carbon nanotube-inserted nitrogen-doped carbon concave-polyhedrons synthesized by direct pyrolysis of bimetallic zeolitic imidazolate framework precursors under a flow of Ar/H_2 and subsequent calcination for both high-performance rechargeable Li-ion and Na-ion batteries. In this structure, Co_3ZnC nanoparticles were homogeneously distributed in in situ growth carbon nanotube-inserted nitrogen-doped carbon concave-polyhedrons. Such a hierarchical structure offers a synergistic effect to withstand the volume variation and inhibit the aggregation of Co_3ZnC nanoparticles during long-term cycles. Meanwhile, the nitrogen-doped carbon and carbon nanotubes in the hierarchical Co_3ZnC/carbon composite offer fast electron transportation to achieve excellent rate capability. As anode of Li-ion batteries, the electrode delivered a high reversible capacity (~800 mA h/g at 0.5 A/g), outstanding high-rate capacity (408 mA h/g at 5.0 A/g), and long-term cycling performance (585 mA h/g after 1500 cycles at 2.0 A/g). In Na-ion batteries, the Co_3ZnC/carbon composite maintains a stable capacity of 386 mA h/g at 1.0 A/g without obvious decay over 750 cycles and a superior rate capability (~500, 448, and 415 mA h/g at 0.2, 0.5, and 1.0 A/g, respectively).

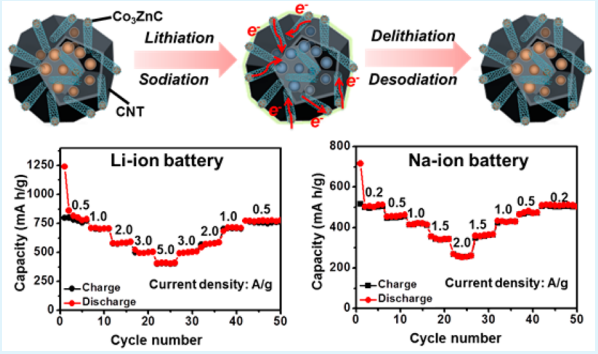

KEYWORDS: *lithium storage, sodium storage, anode materials, ternary metallic carbides, metal−organic frameworks*

INTRODUCTION

Owing to the high capacity, long cycle life, and eco-friendliness, rechargeable lithium-ion batteries (LIBs) and sodium-ion batteries (SIBs) have been regarded as promising energy storage devices for applications in portable electronics and hybrid vehicles.[1−4] However, the energy density, power density, and cycle lifespan of LIBs and SIBs still need to be further improved for fulfilling the urgent demands of society. Massive efforts have been focused on the seeking of novel high-performance anode materials. In this regard, transition-metal oxides (SnO_2,[5−7] MoO_3,[8,9] and Fe_2O_3[10,11]), transition-metal sulfides (SnS_2,[12,13] MoS_2[14−17]) and lithium-alloying materials (Si,[18] Ge[19] and Sn[20]) have been extensively investigated recently. Nevertheless, lithium and sodium storage mechanisms of these materials are mostly based on conversion reaction mechanisms, which could lead to large volume expansion and formation of solid-electrolyte interphase (SEI) layers that may greatly restrict the cycling stability and rate capability.[8,14]

Recently, emerging transition-metal carbides (TMCs) appear to be promising candidates in electrochemical applications because of their high electrical conductivity, excellent stability and inexpensiveness.[21] As expected, some instructive works exploring TMCs as promising anode materials for LIBs have been reported, including Nb_2C,[22] V_2C,[23] Ti_2C,[24] and Ti_3C_2,[25] evidenced by density functional theory (DFT) computations and experiments. Unfortunately, these simple TMCs exhibited relatively low reversible capacity and poor cyclic performance. One appealing approach for improving the cyclic performance is to design TMC/C composite nanostructures, such as Fe_3C embedded in nitrogen-doped carbon,[26] hierarchical porous Mo_2C−C hybrid[27] and core−shell Fe@Fe_3C/C nanocomposites.[28] Besides, the design of hybrid ternary TMC nanostructures is also another possible strategy to promote the reaction kinetics and achieve superior cycle performance. Recently, Xiao and co-workers reported ternary Co_3ZnC/nitrogen-doped carbon material, in which core−shell Co_3ZnC nanoparticles

Received: July 20, 2016
Accepted: September 14, 2016
Published: September 14, 2016

DOI: 10.1021/acsami.6b08911
ACS Appl. Mater. Interfaces 2016, 8, 26834−26841

were implanted in conductive carbon network, delivering a higher reversible capacity and rate capability.[29] It has been proved that the lithium storage mechanism in carbide-based anodes is not conversion reaction and intercalation mechanism, but rather lithium adsorption model. Although ternary TMC-based nanomaterials show good electrochemical performance for lithium storage, there are very few reports on the rational design of hierarchical TMC/C composites for sodium storage. This is mainly attributed to the inherent larger ionic radius of Na^+ (1.02 Å) than Li^+ (0.69 Å).[30,31] Hence, it remains a major challenge to develop an efficient strategy to prepare TMC-based electrode material for both lithium and sodium storage. More recently, metal−organic frameworks (MOFs) have been employed to fabricate carbon-based porous nanostructures as high-performance anode materials with high surface area and abundant hierarchical pore structures.[32−35] As a class of MOFs, zeolitic imidazolate frameworks (ZIFs) can be used as self-templates for the preparation of metal oxide/nitrogen-doped carbon composites due to the abundant carbon and nitrogen species.[36−38] However, the use of bimetallic ZIFs as precursors to prepare TMC/carbon composites for both lithium and sodium storage has not been reported so far.

Herein, we put forward a facile and efficient methode to fabricate novel hierarchical Co_3ZnC/carbon nanotube-inserted N-doped carbon concave-polyhedrons (Co_3ZnC/CNT-NCCPs) by direct pyrolysis of bimetallic ZIFs. In the hierarchical Co_3ZnC/CNT-NCCPs nanostructure, ultrafine Co_3ZnC nanoparticles are evenly embedded in N-doped carbon concave-polyhedrons (NCCPs) or located in the tips of in situ formed CNTs that inserted in the NCCPs. The Co species served as the catalyst for CNT growth on the surface of carbon concave-polyhedrons. In this unique structure, the conductive carbon matrix can effectively accommodate the volume variation and restrict the aggregation of Co_3ZnC during cycling. The porous structure and interconnected CNTs are very beneficial to the electrolyte diffusion and electron transport. With the merits of the hierarchical structure, the Co_3ZnC/CNT-NCCPs exhibit high specific capacities, excellent rate performances and long cycling stabilities as anode materials for both lithium and sodium storage.

RESULTS AND DISCUSSION

The synthesis process of Co_3ZnC/CNT-NCCPs is shown in Scheme 1. First, unique bimetallic ZIF/polyvinylpyrrolidone (PVP) polyhedrons were prepared through a facile room-temperature coprecipitation reaction.[32] Then, the ZIF/PVP polyhedrons were heated to 600 °C under Ar/H_2 flow for 60 min and subsequently calcinated at 600 °C in Ar atmosphere for 360 min to form Co_3ZnC/CNT-NCCP hybrid structure. It should be emphasized that pure Co_3ZnC phase cannot be formed at higher or lower than 600 °C.[29] During the pyrolysis process, the organic linkers (2-methylimidazole) of bimetallic ZIFs and PVP molecules were converted to N-doped porous carbon networks. The partial conversion of ZIFs to tiny Co nanoparticles under a reductive atmosphere could catalyze the formation of CNTs, which significantly improved the conductivity of the resultant product. During the thermal treatment process, the organic ligands of ZIFs and PVP molecules provided carbon source for the formation of Co_3ZnC, and also prevented the aggregation of the Co_3ZnC nanoparticles.

Scheme 1. Schematic Illustration of the Synthesis of Co_3ZnC/CNT-NCCPs

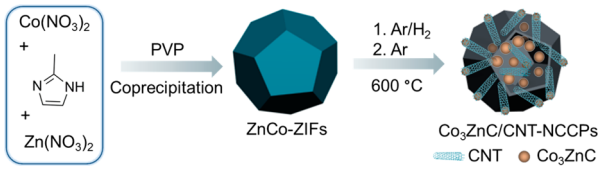

The morphological and structural features of Co_3ZnC/CNT-NCCPs were further characterized by SEM and TEM. A typical SEM image of precursor ZnCo-ZIF/PVP polyhedrons is presented in Figure S1, showing polyhedrons with uniform size and smooth surface. Notably, the as-prepared Co_3ZnC/CNT-NCCPs after thermal treatments well inherited the overall polyhedral morphology and size of bimetallic ZIF precursor (Figure 1a). Nevertheless, the surface of Co_3ZnC/CNT-NCCPs underwent slight shrinkage and became concave, indicating the presence of porous structure after the carbonation process (Figure 1b). As observed in the magnified SEM image (Figure 1c), the short CNTs were grown on the rough surface of Co_3ZnC/CNT-NCCPs, while many Co_3ZnC nanoparticles were encapsulated in the tips of CNTs. It is very likely that Co species have served as the catalyst to grow CNTs during the pyrolysis. The H_2 atmosphere plays a crucial role in the growth of CNTs during the heat treatment. In this process, Co^{2+} ions were partially reduced to Co-based nanoparticles with the assistance of H_2 flow, accompanied by the simultaneous pyrolysis of imidazole ligands to N-doped carbon species. It is known that the Co-based nanocatalysts can serve as highly effective catalyst for the formation of CNTs in the reductive atmosphere.[39,40] In our case, Co based nanoparticles further catalyzed the reconstruction of N-doped carbon species to form N-doped CNTs on the surface of NCCPs. It can be deduced that the in situ growth of CNTs follows the tip-growth mechanism, since the Co-based catalyst nanoparticles are embedded on the tip of CNTs (Figure 1c). The polyhedron shells with interconnected CNTs can enlarge electrolyte/electrode interfaces and facilitate electrochemical active adsorption of lithium or sodium ions.[41] The TEM image of an individual Co_3ZnC/CNT-NCCP reveals that it possesses a porous structure (Figure 1d), in which the Co_3ZnC nanoparticles are encapsulated in the N-doped carbon concave-polyhedrons and in the tips of CNTs (Figure 1e). The Co_3ZnC nanoparticles possess a size distribution between 2−16 nm and an average diameter of ∼8.6 nm (Figure S2). The high-resolution TEM (HRTEM) result reveals that the *d*-spacing of the inserted CNTs is about 0.36 nm, which is in accordance with the (002) planes of graphitic carbon (Figure 1f). The CNTs grown on the concave surface of Co_3ZnC/CNT-NCCPs could effectively improve the electron transport and ion conductivity.

The crystalline nature of each sample was investigated by powder X-ray diffraction (XRD). The XRD pattern of precursor ZnCo-ZIF/PVP polyhedrons exhibited zeolite-type structure with high crystallinity, as shown in Figure S1. Upon carbonization, the resultant Co_3ZnC/CNT-NCCPs show typical interplanar spacings of (111), (200), and (220) facets indexed to cubic Co_3ZnC (JCPDS No. 29-0524) (Figure 2a).[29] Raman spectroscopy was performed to identify the structure of carbon in the Co_3ZnC/CNT-NCCPs (Figure S3a). As expected, two prominent peaks around 1339 and 1589 cm^{-1} were assigned to the D band and G band of carbon,

DOI: 10.1021/acsami.6b08911
ACS Appl. Mater. Interfaces 2016, 8, 26834−26841

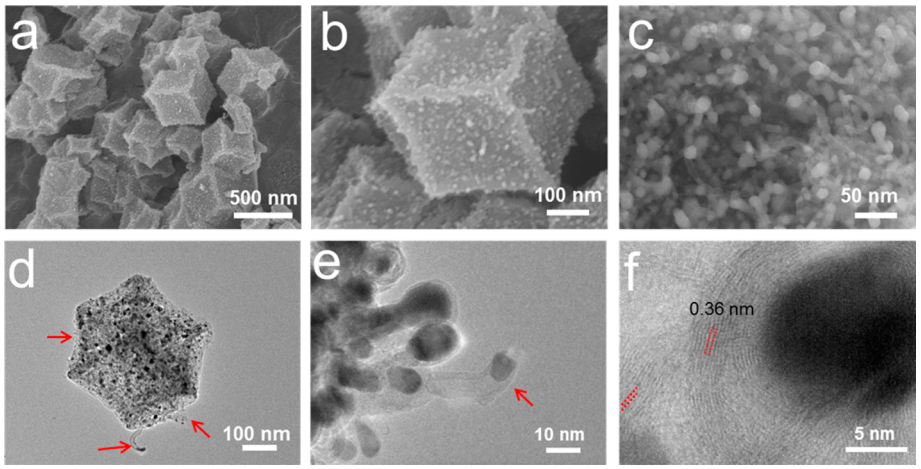

Figure 1. (a–c) SEM, (d,e) TEM, and (f) HRTEM images of Co_3ZnC/CNT-NCCPs.

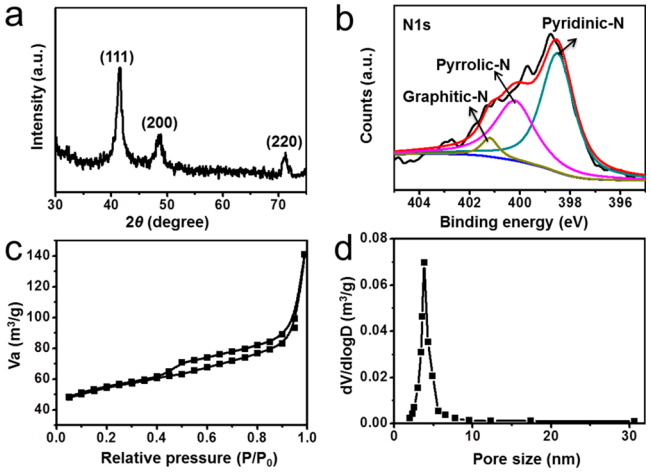

Figure 2. (a) XRD pattern, (b) high-resolution XPS spectrum of N 1s region, (c) nitrogen adsorption–desorption isotherm, and (d) BJH pore size distribution of Co_3ZnC/CNT-NCCPs.

respectively. The band intensity ratio (I_D/I_G) is as high as 1.23, showing structural distortion generated by the existence of N-doping and defects.[42] X-ray photoelectron spectrum (XPS) of Co_3ZnC/CNT-NCCPs demonstrated the presence of Co, Zn, C, and N species (Figure S3b). The high-revolution N 1s peak can be deconvolved into three types of nitrogen species, including pyridinic nitrogen (3.9 at. %) at 398.5 eV, pyrrolic nitrogen (2.8 at. %) at 399.3 eV and graphitic nitrogen (1.5 at. %) at 401.3 eV. In the XPS spectrum of Co 2p region (Figure S3c), two prominent peaks at binding energy of 781.1 eV for $Co2p_{3/2}$ and 796.2 eV for Co $2p_{1/2}$ were observed, respectively. The high-resolution C 1s peak also reveals the existence of C–C bond at 284.5 eV, C═N bond at 285.5 eV and C–N bond at 287.3 eV (Figure S3d). On the basis of energy-dispersive X-ray spectroscopy (EDX), the elemental contents by weight in Co_3ZnC/CNT-NCCPs were determined to be 46.3 wt % Co, 17.5 wt % Zn, 8.6 wt % N, and 27.6 wt % C (Figure S4). The atomic ratio of Co and Zn was found to be 2.93:1, consistent with the stoichiometric ratio of Co_3ZnC phase. The porosity of Co_3ZnC/CNT-NCCPs was further measured by the nitrogen absorption–desorption isotherms. As shown in Figure 2c, the isotherm exhibits a type *IV* behavior with a hysteresis loop between P/P_0 = 0.45 to 1, implying the existence of mesoporous structure. The Brunauer–Emmett–Teller (BET) surface area calculated from the isotherms is 87 cm^2/g, and the pore size is about 3.6 nm based on Barrett–Joyner–Halenda (BJH) method (Figure 2c,d). The existence of hierarchical porous structure in the Co_3ZnC/CNT-NCCPs could promote the diffusion and adsorption of Li^+ and Na^+ ions.

Owing to the unique hierarchical architecture composed of CNT-wrapped N-doped carbon networks with confined Co_3ZnC nanoparticles, the as-prepared product was expected to be useful in LIBs and SIBs. First, enriched N-containing species (such as pyrrolic N and pyridinic N) and evenly dispersed Co_3ZnC nanoparticles can provide plenty of electrochemical active sites for enhanced lithium and sodium storage.[43] Second, the hierarchical porous structure can facilitate the diffusion and mass transfer of electrolyte, as well as alleviate the volume expansion during cycling. Besides, the N-doped carbon matrix and CNTs in the Co_3ZnC/CNT-NCCPs can also enhance the electronic conductivity, which is beneficial to the rate performance.

The electrochemical performance of as-prepared Co_3ZnC/CNT-NCCPs for lithium storage was investigated. Figure 3a shows the cyclic voltammetry (CV) curves in terms of lithium storage for the first three cycles in the potential window of 0.01–3.0 V with a sweep rate of 0.1 mV/s. The cathodic peak around 0.66 V appeared in the first cycle, which was ascribed to the decomposition of electrolyte and the formation of SEI film.[44,45] Figure 3b displays the charge/discharge voltage profiles of the Co_3ZnC/CNT-NCCPs at the first three cycles in a potential window of 0.01–3.0 V (vs Li/Li^+) at a current density of 0.5 A/g. The initial discharge and charge capacities of ~1100 and ~800 mA h/g are calculated based on the total weight of Co_3ZnC/CNT-NCCPs, respectively. The initial irreversible capacity loss of ~27% were observed, which was mainly resulted from the formation of SEI layer and reductive decomposition of the electrolyte. The reversible capacity reached up to 805 mA h/g in the second cycle and stabilized at 770 mA h/g in the 10th cycle, and the Coulombic efficiencies were as high as 89% and 96%, respectively. This result further demonstrates the good reversible Li^+ insertion/extraction property of the anode. Figure 3c shows the cycling performance of the Co_3ZnC/CNT-NCCPs at a current density of 0.5 A/g. The Co_3ZnC/CNT-NCCP based anode shows superior cycling performance with a discharge capacity of 754 mA h/g after 200 cycles.

DOI: 10.1021/acsami.6b08911
ACS Appl. Mater. Interfaces 2016, 8, 26834–26841

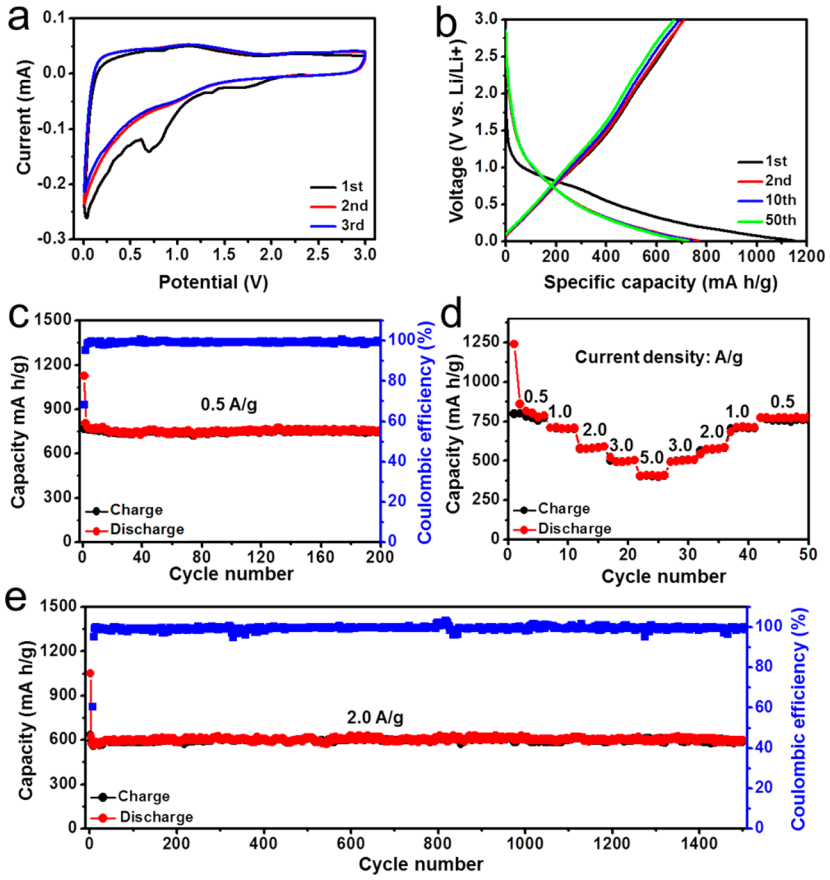

Figure 3. Electrochemical performance of Co_3ZnC/CNT-NCCP based anode for lithium storage. (a) Cyclic voltammetry curves at a scan rate of 0.1 mV/s in the voltage range of 0.01−3.0 V. (b) Galvanostatic charge/discharge profiles of Co_3ZnC/CNT-NCCPs tested at a current density of 0.5 A/g. (c) Cycle performance of Co_3ZnC/CNT-NCCPs at 0.5 A/g, and (d) rate performance of Co_3ZnC/CNT-NCCPs measured at various rates from 0.5 to 5.0 A/g. (e) Long-term cycling stability of Co_3ZnC/CNT-NCCP based anode at a current density of 2.0 A/g.

Meanwhile, it is worthwhile to emphasize that Co_3ZnC/CNT-NCCPs exhibit high rate capability and durable cycle life. The rate capability of Co_3ZnC/CNT-NCCPs was investigated by testing charge/discharge current density from 0.5 to 5.0 A/g, as shown in Figure 3d. Remarkably, the Co_3ZnC/CNT-NCCPs show superior rate performance with average discharge capacities of 810, 708, 585, and 510 mA h/g at current densities of 0.5, 1.0, 2.0, and 3.0 A/g, respectively. Even at the high current density of 5.0 A/g, Co_3ZnC/CNT-NCCP based electrode could still deliver a capacity of 408 mA h/g. After high-rate charge/discharge cycling at 5.0 A/g, the specific capacity can still recover to 780 mA h/g at 0.5 A/g, with the capacity retention of 98% and Coulombic efficiency of 99%. Moreover, the electrode exhibits long-term cycling stability at high current density (Figure 3e). The Co_3ZnC/CNT-NCCP based anode can exhibit a reversible capacity as high as 585 mA h/g after 1500 discharge/charge cycles at 2.0 A/g, showing a high capacity retention with Coulombic efficiency of ∼99%. This result indicates the excellent rate performance and long-term cycling stability of Co_3ZnC/CNT-NCCP based electrode in term of LIBs. The outstanding performances can be assigned to the unique hierarchical structure with nanosized Co_3ZnC nanoparticles and CNTs inserted in the mesoporous nitrogen-doped carbon polyhedrons, which can promote the ion diffusion and reduce the absolute stress/strain during cycling. The superior high-rate capability and cycling performance of Co_3ZnC/CNT-NCCP are summarized in Table S1. To evaluate the energy density for practical applications, the areal loading of Co_3ZnC/CNT-NCCPs was further increased to 3.5 mg/cm^2. Figure S5 shows the cycling performance of Co_3ZnC/CNT-NCCP based electrode at 0.5 A/g. The electrode exhibited an initial discharge capacity of 1019 mA h/g and retained a stable capacity of 704 mA h/g even after 100 cycles, corresponding to an areal capacity of 2.46 mAh/cm^2.

To date, very few TMC nanostructures have been reported as anode materials for sodium storage. In this study, we found that Co_3ZnC/CNT-NCCP based anode could exhibit excellent electrochemical performances in SIBs. The galvanostatic discharge/charge process of Co_3ZnC/CNT-NCCP based anode in $NaClO_4$/propylene carbonate (PC) electrolyte at the first, second and 50th cycles was measured in the potential window of 0.01−3.0 V (vs Na/Na^+) at a current density of 0.2 A/g as shown in Figure 4a. The initial discharge and charge capacities of Co_3ZnC/CNT-NCCPs were 756 and 506 mA h/g, respectively, corresponding to Coulombic efficiency of ∼67%. In the subsequent second cycle, the capacity reached as high as 495 mA h/g and maintained at 485 mA h/g in the 50th cycle, implying the high reversibility of Co_3ZnC/CNT-NCCP based anode. Notably, the high Coulombic efficiency suggests that the CNT-inserted N-doped carbon concave-polyhedrons can effectively mitigate the adverse reactions with electrolyte solution.

The cycling performance of Co_3ZnC/CNT-NCCPs during Na^+ insertion/extraction process was evaluated at a current density of 0.2 A/g for 200 cycles. As shown in Figure 4b, a discharge capacity of ∼500 mA h/g was stably maintained after

DOI: 10.1021/acsami.6b08911
ACS Appl. Mater. Interfaces 2016, 8, 26834−26841

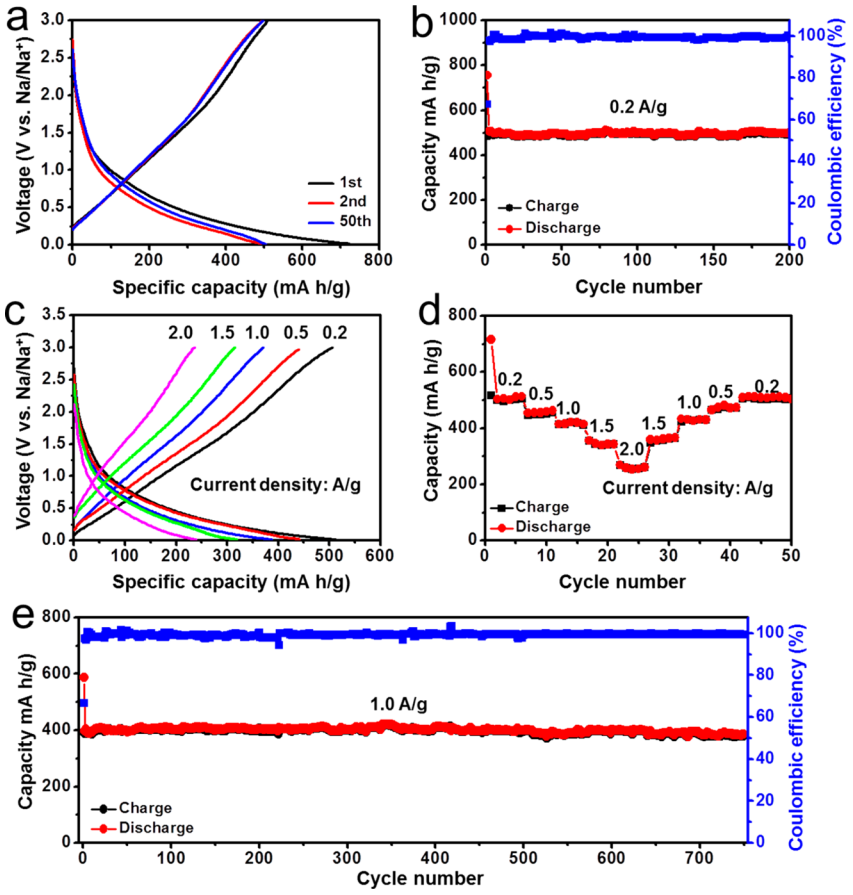

Figure 4. Electrochemical performance of Co_3ZnC/CNT-NCCP based anode for sodium storage. (a) Typical charge/discharge profiles of Co_3ZnC/CNT-NCCPs at 0.2 A/g. (b) Cycling performance of Co_3ZnC/CNT-NCCPs at 0.2 A/g. (c) Representative charge/discharge profiles of Co_3ZnC/CNT-NCCPs at different current rates. (d) Rate capabilities of Co_3ZnC/CNT-NCCPs measured at various current densities from 0.2 to 2.0 A/g. (e) Long-term cycling stability of Co_3ZnC/CNT-NCCP based anode at a current density of 1.0 A/g.

the second cycle. The Co_3ZnC/CNT-NCCP based electrode still retained more than 98% of the second cycle capacity (504 mA h/g) after 200 discharge/charge cycles. The discharge/charge curves of Co_3ZnC/CNT-NCCPs at various current rates are depicted in Figure 4c, and the electrode also exhibits superior rate capabilities for sodium storage (Figure 4d). It is noted that almost no plateau is observed in the discharge curves for SIBs, which indicates that the sodium storage is not based on conversion reaction mechanism. When the current density increased from 0.2 to 0.5, 1.0, 1.5, and 2.0 A/g, the reversible capacities decreased from 500 to 448, 415, 339, and 255 mA h/g, respectively. The discharge capacity can be recovered to 512 mA h/g upon the reduction of current rate to 0.2 A/g. As expected, these results clearly reveal that the integrated structure of Co_3ZnC/CNT-NCCPs can facilitate the fast and stable sodium storage, and improve the electrochemical performances. To evaluate the long-term cycling performance of Co_3ZnC/CNT-NCCPs, the electrode was cycled at a high current density of 1.0 A/g over 750 cycles (Figure 4e). The discharge capacity of 404 mAh/g in the second cycle is used as a control. The electrodes deliver a discharge capacity as high as 398 mA h/g after 500 cycles with a capacity retention of about 98%. Moreover, a specific capacity of 386 mA h/g was retained even after 750 cycles, and the capacity retention was nearly 95.5% compared to the discharge capacity of the second cycle. These results also confirmed the hierarchical nanostructure with Co_3ZnC nanoparticles embedded in CNT-inserted N-doped carbon concave-polyhedrons contributed to the superior cycling stability and rate performance.

To understand the remarkable kinetic properties of Co_3ZnC/CNT-NCCP based electrode for lithium and sodium storage, electrochemical impedance spectra (EIS) were measured before and after 100 charge/discharge cycles, respectively. As shown in Figure S6, the depressed semicircles are related to the charge-transfer resistance at the electrode/electrolyte interfaces. Clearly, both two Nyquist plots show that the charge transfer resistances after 100 cycles were smaller than those before cycling, which can be attributed to the further wetting and infiltration of electrolyte in the pores of Co_3ZnC/CNT-NCCPs.

The TEM images of Co_3ZnC/CNT-NCCPs upon discharging and charging are shown in Figure S7. In both fully discharged or charged states, the electrode material still maintained the original concave-polyhedral morphology without structural collapse or aggregation of Co_3ZnC nanoparticles. To understand the sodium storage mechanism, the crystalline phase of Co_3ZnC/CNT-NCCPs at fully discharged and charged states were investigated. The HRTEM image after discharged to 0.01 V (Figure S7c) shows a lattice fringe with *d*-spacing of 0.26 nm, consistent well with the (110) planes of cubic Co_3ZnC; When being charged to 3.0 V (Figure S7d), no noticeable change of the lattice fringe is observed. This result demonstrates that the sodium storage mechanism in Co_3ZnC/CNT-NCCPs is mainly determined by sodium adsorption

DOI: 10.1021/acsami.6b08911
ACS Appl. Mater. Interfaces 2016, 8, 26834−26841

model. The prominent electrochemical performance of hierarchical Co_3ZnC/CNT-NCCPs can be ascribed to the unique structural and compositional features: (1) The ultrafine Co_3ZnC nanoparticles and hierarchical pores can serve as efficient reservoirs for storing Li^+/Na^+. (2) The 3D porous carbon matrix can effectively provide smooth pathways for electron transport, accommodate the volume change and prevent the aggregation of Co_3ZnC nanoparticles during cycling. (3) The nitrogen-containing species (pyrrolic and pyridinic nitrogen) can introduce more active sites for adsorbing extra Li^+ or Na^+ and contribute to high lithium- and sodium-storage capacities. (4) The combination of highly conductive CNTs and N-doped carbon matrix not only shorten diffusion distance of Li^+/Na^+ ions but also enhance the electronic conductivity thus improving the rate capabilities.

CONCLUSION

In conclusion, we have developed an efficient ZIF-templated approach to prepare hierarchical Co_3ZnC/CNT-NCCPs, in which ultrafine Co_3ZnC nanoparticles are homogeneously embedded in N-doped carbon polyhedrons or encapsulated in the tips of CNTs grown on the surface of concave-polyhedrons. Such unique composite exhibited excellent lithium- and sodium-storage performance in terms of high capacities, excellent rate capabilities and long-term cycling performance. For lithiation, the electrode exhibited a reversible capacity of 585 mA h/g over 1500 cycles at 2.0 A/g and high rate capability of 408 mA h/g at 5.0 A/g. During sodiation/desodiation process, the as-prepared electrode exhibited a stable desodiation capacity of 386 mA h/g after 750 cycles at 1.0 A/g, and a discharge capacity of 255 mA h/g even at 2.0 A/g. We expect this synthesis strategy can be used for the future development of high-performance LIBs and SIBs.

EXPERIMENTAL SECTION

Synthesis of ZnCo-ZIF/PVP Polyhedrons. ZnCo-ZIF/PVP polyhedrons were synthesized through a simple room-temperature precipitation method. In a typical synthesis, 2-methykimidazole (0.98 g) and PVP (2.0 g) were added in 10 mL of methanol under magnetic stirring. $Co(NO_3)_2{\cdot}6H_2O$ (0.873 g) and $Zn(NO_3)_2{\cdot}6H_2O$ (0.297 g) were dissolved in 30 mL of methanol under stirring. Then, the above two solutions were mixed under continuous stirring for 10 min, and then aged at room temperature for 24 h. The purple powder was obtained through centrifugation, rinsing with ethanol for several times, and vacuum drying at 80 °C overnight.

Synthesis of Co_3ZnC/CNT-NCCPs. The precursor ZnCo-ZIF/PVP polyhedrons were placed in a ceramic boat, and then heated in a tube furnace at a ramp rate of 2 °C/min to 600 °C under Ar/H_2 flow (95%/5% in volume ratio) for 1 h, and then further annealed at 600 °C in argon flow for 6 h. After cooling naturally, the black product was finally collected.

Characterizations. The morphology and structures of samples were characterized by scanning electron microscopy (SEM, HITACH S-4800, 5 kV) and transmission electron microscopy (TEM, JEM-2100, 200 kV). Elemental analysis was performed using energy-dispersive X-ray spectroscopy (EDX) equipped in the SEM. Nitrogen sorption isotherms were measured through Brunauer–Emmett–Teller (BET) analysis on a Quantachrome Autosorb-IQ-2C-TCD-VP analyzer at liquid-nitrogen temperature. Before the BET analysis, the samples were degassed under vacuum at 200 °C for 6 h. Powder X-ray powder diffraction (XRD) spectra were collected using a Shimadzu XRD-6000 diffractometer equipped with a rotating anode and a Cu Kα radiation source (λ = 1.54178 Å). Raman spectra were collected using a Horiba JY Evolution Raman spectrometer with an excitation laser of 532 nm wavelength. X-ray photoelectron spectra (XPS) were collected with a PHI-5000 VersaProbe X-ray photoelectron spectrometer with an Al Kα X-ray radiation.

Electrochemical Measurements. The working electrodes were fabricated with the active materials, conductive Kejten black, and polyvinylidene fluoride (PVDF) in *N*-methyl-2-pyrrolidinone (NMP) solvent with a weight ratio of 85:5:10. The as-obtained slurry was then smeared on a copper foil and vacuum-dried at 100 °C for 12 h in vacuum. The area mass loading of active materials ranged from 0.8 and 1.5 mg/cm^2. The cells were assembled in an argon-filled glovebox with levels of moisture and oxygen less than 1 ppm. For the fabrication of LIBs, CR 2032 coin-type cells were assembled with lithium foils as counter electrodes, Celgard 2400 membranes as separators, and 1.0 M $LiPF_6$ in a cosolvent of ethylene carbonate and dimethyl carbonate (1:1 by volume) as electrolyte. The fabrication of SIBs is similar to that of LIBs, but sodium foils were used as counter electrodes and a solution of 1.0 M $NaClO_4$ in propylene carbonate (PC) with 5 wt % fluoroethylene carbonate (FEC) was used as electrolyte. The galvanostatic charge–discharge performances were measured on a LAND CT2001A multichannel battery test system between 0.01–3.0 V at room temperature. The specific capacity is calculated based on the total mass of active materials. The cyclic voltammetry (CV) tests were carried out on a Chenhua CHI-760 electrochemical workstation.

ASSOCIATED CONTENT

Supporting Information

The Supporting Information is available free of charge on the ACS Publications website at DOI: 10.1021/acsami.6b08911.

SEM image and XRD pattern of ZnCo-ZIF/PVP polyhedrons, size analysis of Co_3ZnC nanoparticles embedded in Co_3ZnC/CNT-NCCPs, Raman spectrum, XPS spectrum and high-resolution XPS spectra of Co 2p and C 1s regions, SEM image and EDX spectrum and elemental content analysis of Co_3ZnC/CNT-NCCPs, comparison of the results in this work with reported performance of Co_3ZnC/C–N hybrid as anode materials for lithium storage, cycling performance of Co_3ZnC/CNT-NCCP electrode with a high areal loading of 3.5 mg/cm^2 for lithium storage at 0.5 A/g, Nyquist plots of Co_3ZnC/CNT-NCCPs and TEM images of Co_3ZnC/CNT-NCCPs upon discharging to 0.01 V and charging to 3.0 V (PDF)

AUTHOR INFORMATION

Corresponding Authors

*Phone: +86-18115605182. E-mail: zhongjin@nju.edu.cn.
*Phone: +1-919-660-1549. E-mail: j.liu@duke.edu.

Notes

The authors declare no competing financial interest.

ACKNOWLEDGMENTS

This work is supported by the National Thousand Young Talents Program of China, the Young Scientists Project of National Basic Research Program of China (973 Program No. 2015CB659300), the National Natural Science Foundation of China (NSFC Grant No. 21403105 and No. 21573108), the China Postdoctoral Science Foundation (Grant No. 2015M581768 and No. 2015M580413), the Natural Science Foundation for Young Scholars of Jiangsu Province (Grant No. BK20150583), the Fundamental Research Funds for the Central Universities (Grant No. 020514380073 and No. 020514380079) and a project funded by the Priority Academic Program Development of Jiangsu Higher Education Institutions (PAPD).

DOI: 10.1021/acsami.6b08911
ACS Appl. Mater. Interfaces 2016, 8, 26834–26841

REFERENCES

(1) Palacin, M. R. Recent Advances in Rechargeable Battery Materials: A Chemist's Perspective. *Chem. Soc. Rev.* **2009**, *38*, 2565−2575.

(2) Ebner, M.; Marone, F.; Stampanoni, M.; Wood, V. Visualization and Quantification of Electrochemical and Mechanical Degradation in Li Ion Batteries. *Science* **2013**, *342*, 716−720.

(3) Van Noorden, R. The Rechargeable Revolution: A Better Battery. *Nature* **2014**, *507*, 26−28.

(4) Wang, Y. R.; Chen, R. P.; Chen, T.; Lv, H. L.; Zhu, G. Y.; Ma, L. B.; Wang, C. X.; Jin, Z.; Liu, J. Emerging Non-Lithium Ion Batteries. *Energy Storage Mater.* **2016**, *4*, 103−129.

(5) Zhou, X.; Wan, L. J.; Guo, Y. G. Binding SnO_2 Nanocrystals in Nitrogen-Doped Graphene Sheets as Anode Materials for Lithium-Ion Batteries. *Adv. Mater.* **2013**, *25*, 2152−2157.

(6) Hong, Y. J.; Son, M. Y.; Kang, Y. C. One-Pot Facile Synthesis of Double-Shelled SnO_2 Yolk-Shell-Structured Powders by Continuous Process as Anode Materials for Li-Ion Batteries. *Adv. Mater.* **2013**, *25*, 2279−2283.

(7) Zhao, Y.; Wei, C.; Sun, S.; Wang, L. P.; Xu, Z. J. Reserving Interior Void Space for Volume Change Accommodation: An Example of Cable-Like MWNTs@SnO_2@C Composite for Superior Lithium and Sodium Storage. *Adv. Sci.* **2015**, *2*, 1500097.

(8) Meduri, P.; Clark, E.; Kim, J. H.; Dayalan, E.; Sumanasekera, G. U.; Sunkara, M. K. MoO_{3-x} Nanowire Arrays as Stable and High-Capacity Anodes for Lithium Ion Batteries. *Nano Lett.* **2012**, *12*, 1784−1788.

(9) Ko, Y. N.; Park, S. B.; Jung, K. Y.; Kang, Y. C. One-Pot Facile Synthesis of Ant-Cave-Structured Metal Oxide-Carbon Microballs by Continuous Process for Use as Anode Materials in Li-Ion Batteries. *Nano Lett.* **2013**, *13*, 5462−5466.

(10) Lin, J.; Raji, A. R. O.; Nan, K.; Peng, Z.; Yan, Z.; Samuel, E. L. G.; Natelson, D.; Tour, J. M. Iron Oxide Nanoparticle and Graphene Nanoribbon Composite as an Anode Material for High-Performance Li-Ion Batteries. *Adv. Funct. Mater.* **2014**, *24*, 2044−2048.

(11) Zhang, N.; Han, X. P.; Liu, Y. C.; Hu, X. F.; Zhao, Q.; Chen, J. 3D Porous gamma-Fe_2O_3@C Nanocomposite as High-Performance Anode Material of Na-Ion Batteries. *Adv. Energy Mater.* **2015**, *5*, 1401123.

(12) Zhang, Y. D.; Zhu, P. Y.; Huang, L. L.; Xie, J.; Zhang, S. C.; Cao, G. S.; Zhao, X. B. Few-Layered SnS_2 on Few-Layered Reduced Graphene Oxide as Na-Ion Battery Anode with Ultralong Cycle Life and Superior Rate Capability. *Adv. Funct. Mater.* **2015**, *25*, 481−489.

(13) Seo, J. W.; Jang, J. T.; Park, S. W.; Kim, C.; Park, B.; Cheon, J. Two-Dimensional SnS_2 Nanoplates with Extraordinary High Discharge Capacity for Lithium Ion Batteries. *Adv. Mater.* **2008**, *20*, 4269−4273.

(14) David, L.; Bhandavat, R.; Singh, G. MoS_2/Graphene Composite Paper for Sodium-Ion Battery Electrodes. *ACS Nano* **2014**, *8*, 1759−1770.

(15) Hu, Z.; Wang, L.; Zhang, K.; Wang, J.; Cheng, F.; Tao, Z.; Chen, J. MoS_2 Nanoflowers with Expanded Interlayers as High-Performance Anodes for Sodium-Ion Batteries. *Angew. Chem.* **2014**, *126*, 13008−13012.

(16) Yang, L. C.; Wang, S. N.; Mao, J. J.; Deng, J. W.; Gao, Q. S.; Tang, Y.; Schmidt, O. G. Hierarchical MoS_2/Polyaniline Nanowires with Excellent Electrochemical Performance for Lithium-Ion Batteries. *Adv. Mater.* **2013**, *25*, 1180−1184.

(17) Zhu, C.; Mu, X.; van Aken, P. A.; Yu, Y.; Maier, J. Single-Layered Ultrasmall Nanoplates of MoS_2 Embedded in Carbon Nanofibers with Excellent Electrochemical Performance for Lithium and Sodium Storage. *Angew. Chem., Int. Ed.* **2014**, *53*, 2152−2156.

(18) Liu, N.; Lu, Z. D.; Zhao, J.; McDowell, M. T.; Lee, H. W.; Zhao, W. T.; Cui, Y. A Pomegranate-Inspired Nanoscale Design for Large-Volume-Change Lithium Battery Anodes. *Nat. Nanotechnol.* **2014**, *9*, 187−192.

(19) Chan, C. K.; Zhang, X. F.; Cui, Y. High Capacity Li Ion Battery Anodes Using Ge Nanowires. *Nano Lett.* **2008**, *8*, 307−309.

(20) Huang, X. K.; Cui, S. M.; Chang, J. B.; Hallac, P. B.; Fell, C. R.; Luo, Y. T.; Metz, B.; Jiang, J. W.; Hurley, P. T.; Chen, J. H. A Hierarchical Tin/Carbon Composite as an Anode for Lithium-Ion Batteries with a Long Cycle Life. *Angew. Chem., Int. Ed.* **2015**, *54*, 1490−1493.

(21) Tang, Q.; Zhou, Z.; Shen, P. Are MXenes Promising Anode Materials for Li Ion Batteries? Computational Studies on Electronic Properties and Li Storage Capability of Ti_3C_2 and $Ti_3C_2X_2$ (X = F, OH) Monolayer. *J. Am. Chem. Soc.* **2012**, *134*, 16909−16916.

(22) Naguib, M.; Halim, J.; Lu, J.; Cook, K. M.; Hultman, L.; Gogotsi, Y.; Barsoum, M. E. New Two-Dimensional Niobium and Vanadium Carbides as Promising Materials for Li-Ion Batteries. *J. Am. Chem. Soc.* **2013**, *135*, 15966−15969.

(23) Lukatskaya, M. R.; Mashtalir, O.; Ren, C. E.; Dall'Agnese, Y.; Rozier, P.; Taberna, P. L.; Naguib, M.; Simon, P.; Barsoum, M. W.; Gogotsi, Y. Cation Intercalation and High Volumetric Capacitance of Two-Dimensional Titanium Carbide. *Science* **2013**, *341*, 1502−1505.

(24) Mashtalir, O.; Naguib, M.; Mochalin, V. N.; Dall'Agnese, Y.; Heon, M.; Barsoum, M. W.; Gogotsi, Y. Intercalation and Delamination of Layered Carbides and Carbonitrides. *Nat. Commun.* **2013**, *4*, 1716.

(25) Naguib, M.; Come, J.; Dyatkin, B.; Presser, V.; Taberna, P. L.; Simon, P.; Barsoum, M. W.; Gogotsi, Y. MXene: A Promising Transition Metal Carbide Anode for Lithium-Ion Batteries. *Electrochem. Commun.* **2012**, *16*, 61−64.

(26) Zhao, X.; Xia, D.; Yue, J.; Liu, S. *In-Situ* Generated Nano-Fe_3C Embedded into Nitrogen-Doped Carbon for High Performance Anode in Lithium Ion Battery. *Electrochim. Acta* **2014**, *116*, 292−299.

(27) Xiao, Y.; Zheng, L.; Cao, M. Hybridization and Pore Engineering for Achieving High-Performance Lithium Storage of Carbide as Anode Material. *Nano Energy* **2015**, *12*, 152−160.

(28) Su, L.; Zhou, Z.; Shen, P. Core-shell Fe@Fe_3C/C Nanocomposites as Anode Materials for Li Ion Batteries. *Electrochim. Acta* **2013**, *87*, 180−185.

(29) Xiao, Y.; Sun, P. P.; Cao, M. H. Core-Shell Bimetallic Carbide Nanoparticles Confined in a Three-Dimensional N-Doped Carbon Conductive Network for Efficient Lithium Storage. *ACS Nano* **2014**, *8*, 7846−7857.

(30) Wen, Y.; He, K.; Zhu, Y. J.; Han, F. D.; Xu, Y. H.; Matsuda, I.; Ishii, Y.; Cumings, J.; Wang, C. S. Expanded Graphite as Superior Anode for Sodium-Ion Batteries. *Nat. Commun.* **2014**, *5*, 4033.

(31) Slater, M. D.; Kim, D.; Lee, E.; Johnson, C. S. Sodium-Ion Batteries. *Adv. Funct. Mater.* **2013**, *23*, 947−958.

(32) Wu, R.; Qian, X.; Zhou, K.; Wei, J.; Lou, J.; Ajayan, P. M. Porous Spinel $Zn_xCo_{3-x}O_4$ Hollow Polyhedra Templated for High-Rate Lithium-Ion Batteries. *ACS Nano* **2014**, *8*, 6297−6303.

(33) Zou, F.; Hu, X. L.; Li, Z.; Qie, L.; Hu, C. C.; Zeng, R.; Jiang, Y.; Huang, Y. H. MOF-Derived Porous ZnO/$ZnFe_2O_4$/C Octahedra with Hollow Interiors for High-Rate Lithium-Ion Batteries. *Adv. Mater.* **2014**, *26*, 6622−6628.

(34) Zhang, L.; Wu, H. B.; Lou, X. W. Metal-Organic-Frameworks-Derived General Formation of Hollow Structures with High Complexity. *J. Am. Chem. Soc.* **2013**, *135*, 10664−10672.

(35) Chen, T.; Hu, Y.; Cheng, B. R.; Chen, R. P.; Lv, H. L.; Ma, L. B.; Zhu, G. Y.; Wang, Y. R.; Yan, C. Z.; Tie, Z. X.; Jin, Z.; Liu, J. Multi-Yolk-Shell Copper Oxide@Carbon Octahedra as High-Stability Anodes for Lithium-Ion Batteries. *Nano Energy* **2016**, *20*, 305−314.

(36) Liu, J.; Wu, C.; Xiao, D.; Kopold, P.; Gu, L.; van Aken, P. A.; Maier, J.; Yu, Y. MOF-Derived Hollow Co_9S_8 Nanoparticles Embedded in Graphitic Carbon Nanocages with Superior Li-Ion Storage. *Small* **2016**, *12*, 2354−2364.

(37) Aijaz, A.; Masa, J.; Rösler, C.; Xia, W.; Weide, P.; Botz, A. J. R.; Fischer, R. A.; Schuhmann, W.; Muhler, M. Co@Co_3O_4 Encapsulated in Carbon Nanotube-Grafted Nitrogen-Doped Carbon Polyhedra as an Advanced Bifunctional Oxygen Electrode. *Angew. Chem., Int. Ed.* **2016**, *55*, 4087−4091.

(38) Wang, Q.; Zou, R.; Xia, W.; Ma, J.; Qiu, B.; Mahmood, A.; Zhao, R.; Yang, Y.; Xia, D. G.; Xu, Q. Facile Synthesis of Ultrasmall CoS_2

DOI: 10.1021/acsami.6b08911
ACS Appl. Mater. Interfaces 2016, 8, 26834−26841

Nanoparticles within Thin N-Doped Porous Carbon Shell for High Performance Lithium-Ion Batteries. *Small* **2015**, *11*, 2511−2517.
(39) Yuan, D.; Ding, L.; Chu, H.; Feng, Y.; McNicholas, T. P.; Liu, J. Horizontally Aligned Single-Walled Carbon Nanotube on Quartz from a Large Variety of Metal Catalysts. *Nano Lett.* **2008**, *8*, 2576−2579.
(40) Yang, F.; Wang, X.; Zhang, D. Q.; Yang, J.; Luo, D.; Xu, Z. W.; Wei, J. K.; Wang, J. Q.; Xu, Z.; Peng, F.; Li, X. M.; Li, R. M.; Li, Y. L.; Li, M. H.; Bai, X. D.; Ding, F.; Li, Y. *Nature* **2014**, *510*, 522−524.
(41) Huang, G.; Zhang, F. F.; Du, X. C.; Qin, Y. L.; Yin, D. M.; Wang, L. M. Metal Organic Frameworks Route to *In Situ* Insertion of Multiwalled Carbon Nanotubes in Co_3O_4 Polyhedra as Anode Materials for Lithium-Ion Batteries. *ACS Nano* **2015**, *9*, 1592−1599.
(42) Ferrari, A. C.; Basko, D. M. Raman Spectroscopy as a Versatile Tool for Studying the Properties of Graphene. *Nat. Nanotechnol.* **2013**, *8*, 235−246.
(43) Yao, F.; Güneş, F.; Ta, H. Q.; Lee, S. M.; Chae, S. J.; Sheem, K. Y.; Cojocaru, C. S.; Xie, S. S.; Lee, Y. H. Diffusion Mechanism of Lithium Ion through Basal Plane of Layered Graphene. *J. Am. Chem. Soc.* **2012**, *134*, 8646−8654.
(44) Wang, H. L.; Cui, L. F.; Yang, Y.; Sanchez Casalongue, H.; Robinson, J. T.; Liang, Y. Y.; Cui, Y.; Dai, H. J. Mn_3O_4-Graphene Hybrid as a High-Capacity Anode Material for Lithium Ion Batteries. *J. Am. Chem. Soc.* **2010**, *132*, 13978−13980.
(45) Lee, S. W.; Yabuuchi, N.; Gallant, B. M.; Chen, S.; Kim, B. S.; Hammond, P. T.; Shao-Horn, Y. High-Power Lithium Batteries from Functionalized Carbon-Nanotube Electrodes. *Nat. Nanotechnol.* **2010**, *5*, 531−537.

DOI: 10.1021/acsami.6b08911
ACS Appl. Mater. Interfaces 2016, 8, 26834−26841